Chapter 2
SYNTHESIS AND CHARACTERIZATIONS

2.1 Introduction

This chapter presents the synthesis method adopted in the preparation of different samples used in our research work, along with various techniques used to characterize and investigate the material. Detailing of the x-ray diffraction, Rietveld refinement technique for analysing crystal structures, and magnetic characterizations have been done. In addition to structural and magnetic analysis., XPS, Raman spectroscopy, UV-visible spectroscopy, and Photoluminescence spectroscopy, valuable tools for studying materials' optical and vibrational properties, are also discussed. Finally, we have discussed the electronic structures studied through density functional theory (DFT). The samples $Dy_2Ti_{2-x}Mn_xO_7$ (x = 0, 0.05, 0.10, 0.15, 0.20) and $Er_2Ti_{2-x}Mn_xO_7$ (x = 0.0, 0.10, 0.15) both crystallize in cubic phase with $Fd\bar{3}m$ space group under ambient preparation conditions, exhibiting pyrochlore structure. The stability-field map illustrates the preparation condition depending upon the ionic radii of A (rare-earth ion) and B (transition metal ion) site elements, as discussed in Section 2.2. Section 2.3 will discuss the synthesis of parent and Mn-doped derivatives of $Dy_2Ti_2O_7$ and $Er_2Ti_2O_7$. Section 2.4 will deal with the characterization techniques used in the present work to study the system properties.

2.2 Stability-field/Structure-stability Map for the synthesis of $A_2B_2O_7$ materials

The pyrochlore structure is the most common structure, which is known to cause geometrical spin frustration. The geometric frustration plays a crucial role in the underlying physics of spin relaxation phenomena. In the pyrochlore $A_2B_2O_7$, the R_A/R_B cation radius ratio determines the phase stability of the pyrochlore lattice over the defect fluorite structure in the lower limit. Under ambient air pressure, the pyrochlores are stable for R_A/R_B, ranging from $1.36 \leq R_A/R_B \leq 1.71$. Although we may find some exceptions, such as the system $Pr_2Ru_2O_7$ is a stable compound with a radius ratio of ~1.82, $Pr_2Mo_2O_7$ is not a stable compound even with a smaller radius ratio of ~1.73. The structure-stability map or structure-field map of pyrochlores in the space of ionic radii is given in **Figure 2.1** [3]. One can notice that the pyrochlore phase is not stable for all A for a given B rather, the deciding factor for stability is the ionic radius ratio R_A^{3+}/ R_B^{4+}. However, it is interesting to note that only B = Sn series can form stable pyrochlore structures with all rare earth ions. For instance, for B ions with small ionic radii, such as Mn^{4+}, a high-pressure method must be undertaken to prepare the stable pyrochlore phases. For pyrochlore families, the first series that is stable under ambient pressure is for B = V. This is only true for the three smallest members, Lu, Yb, and Tm. On the other hand, for the largest B ion, Pb^{4+}, the smallest A ion (rare-earth) for which we get stable pyrochlore is Gd ($Gd_2Pb_2O_7$).

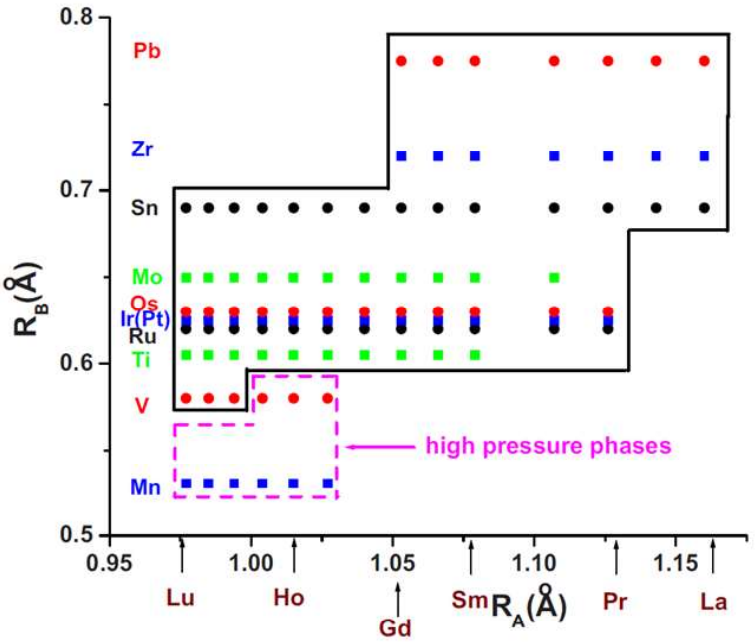

Figure 2.1 Stability field map for the synthesis of $A_2B_2O_7$ magnetically frustrated systems [3]**.**

2.3 Solid-State Synthesis Route

Figure 2.2 shows the flowchart for the stepwise procedure adopted for sample synthesis. The Polycrystalline sample of pure phase $Dy_2Ti_2O_7$, $Er_2Ti_2O_7$, and their doped derivatives, $Dy_2Ti_{2-x}Mn_xO_7$ (x = 0.0, 0.05, 0.10, 0.15, 0.20) and $Er_2Ti_{2-x}Mn_xO_7$ (x = 0.0, 0.05, 0.10, 0.15, 0.20) compounds were synthesized using a conventional solid-state reaction method. The reagents are mixed homogeneously and then heated to facilitate thermochemical reactions between them. Dy_2O_3 (Alfa Aesar 99.99%), Er_2O_3 (99.9% assay, Sigma Aldrich), TiO_2 (Sigma Aldrich 99.8%) and MnO_2 (Alfa Aesar 99.9%) are used as the starting material. The starting material is initially taken in a stoichiometric ratio and set for mechanical mixing in a high-energy ball mill using ethanol as a medium, followed by drying under ambient

conditions. The powder was calcined at 1400 °C for 24 h in an alumina crucible to facilitate thermo-chemical reaction. After that, it was crushed into fine powder in an agate mortar, followed by mixing binder Polyvinyl alcohol (PVA) to make pellets; then, pellets were kept at 600°C to remove the binder and then sintered at 1425 °C for 12 h. Finally, it was crushed and annealed at 600°C for 10 h to remove the introduced strain.

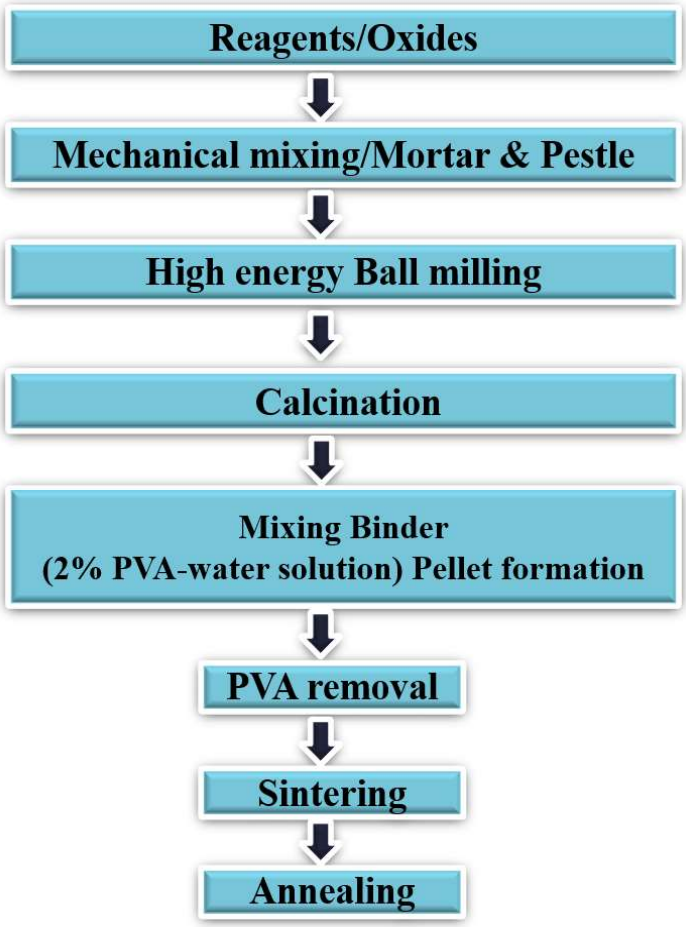

Figure 2.2 Flowchart for standard solid-state route adopted for the sample synthesis.

The phase purity of the as-synthesized sample was confirmed using a room temperature high-resolution x-ray diffractometer (HRXRD) (Smart Lab 9 kW, Rigaku, Japan) having $CuK_{\alpha 1}$

optics close to the source side. The homogenous composition of powdered samples has been used for further characterization. The obtained room temperature HRXRD pattern along with results of Rietveld refinement for $Dy_2Ti_{2-x}Mn_xO_7$ (x = 0.0, 0.05, 0.10, 0.15, 0.20) and $Er_2Ti_{2-x}Mn_xO_7$ (x = 0.0, 0.10, 0.20) is presented in subsequent chapters in section 3.1 and section 5.1 respectively.

2.4 Characterization Techniques:

The following section deals with the various characterization tools adopted for studying the structural, magnetic, electronic, and optical properties of the synthesized samples.

2.4.1 x-ray diffraction

The x-ray diffraction (XRD) technique is an essential and non-destructive technique primarily employed to examine the phase and crystal structure of any crystalline/polycrystalline materials qualitatively and quantitatively. Crystallographic phase identification, phase quantification, crystallinity, crystallite size and strain, lattice parameters, and atomic structure are primarily measured using XRD, as many of the physical characteristics of materials, particularly their electrical, magnetic, and optical properties, are correlated with the arrangement of atoms/ions/molecules on their crystallographic sites.

The XRD works on the basic principle of Bragg's law, which states that the incident x-rays are diffracted from a set of equally spaced lattice planes in the crystal that interfere constructively. These scattered x-rays interfere constructively when the path difference between them is an integral multiple of the x-ray wavelength. This can be mathematically expressed as follows:

$$2d_{hkl} \, Sin\theta = \lambda \quad (2.1)$$

Where d_{hkl} is the interplanar separation for a set of planes having Miller indices (hkl), θ is the angle between the incident/diffracted beam and the corresponding lattice plane, i.e., Bragg's angle, and λ is the wavelength of the x-ray radiation, which is used for diffraction [56]. When the incident radiation satisfies Bragg's law, the diffracted beam will make coherent superposition and high-intensity peaks at certain scattering angles can be recorded using a detector.

In general, the diffraction peaks depend on the symmetry of the structure. Crystals with lower symmetry, say, monoclinic, exhibit several diffraction peaks because of numerous lattice planes, whereas in the case of high symmetric crystal structures, like cubic and tetragonal containing certain lattice planes, a relatively lesser number of diffraction peaks are observed. The nature of diffraction peaks and their intensities are also correlated with the size and shape of particles in the crystal.

In our study, phase purity was examined with a high-resolution x-ray diffraction (HRXRD) pattern obtained using x-ray diffractometer (Smart Lab 9 kW, Rigaku, Japan; Cu $K_{\alpha 1}$ radiation of 1.54059 Å. The XRD patterns are recorded in the range of $2\theta = (10 - 120)°$. Further, we performed Rietveld refinement through FULLPROF SUITE [57] software for structural analysis (space group and lattice parameter) and indexing of HRXRD patterns. In this fitting technique, suitably generated intensities based on the input parameters are matched with experimental data to determine the crystal structure of a specific space group. Other structural parameters like bond lengths and bond angles are obtained using VESTA (3d visualization software) [58]. A brief description of the Rietveld refinement method is described below.

2.4.2 A brief presentation of the Rietveld refinement method:

This programme is employed for structure profile refinement of x-ray powder diffraction data. It also serves the purpose of profile matching of the diffraction pattern without prior knowledge of the structure. In order to extract all the information possible from the diffraction pattern related to the sample, a computer program developed by Dr. H. Rietveld is utilized, known as 'Rietveld refinement', 'Rietveld analysis' or 'Rietveld method' [59], [60].

The refinement iteration is performed until the best fit is obtained between the observed powder diffraction pattern. In this approach, to get the proper structure of any crystalline materials, the experimental diffraction pattern is fitted by the approximated structural model by using least square method. The overall calculated pattern depends on the refined crystal structure model, diffraction optics effect, instrumental factors and other specimen characteristics [61]. To achieve the best fit, we minimise the difference between the theoretical and experimental diffraction patterns to an acceptable level by altering the instrumental and structural refinable parameters. The objective is to minimize the parameter residual, Sy:

$$S_y = \sum_i w_i \, (y_{oi} - y_{ci})^2 \qquad (2.2)$$

where y_{oi} denotes the observed intensity, y_{ci} is the calculated intensity at the i^{th} step of diffraction pattern, and w_i is a suitable weight given by $(w_i)^{-1} = y_{oi}$.

Multiple individual reflections produce a powder diffraction pattern. Each reflection has a peak height, a peak position, a breadth, and an integrated area which is proportional to the Bragg Intensity I_k of each reflection where k represents the Miller indices h, k, l. Intensity I_k is directly proportional to the square of the structure factor ($I_k \alpha |F_k|^2$) [61]. The observed

intensity, y_{oi}, at any arbitrarily chosen point' i' in the powder diffraction pattern arises from the collective contribution from multiple Bragg reflections. The calculated intensities y_{ci} are determined from the equation:

$$y_{ci} = s \sum L_k |F_k|^2 \Phi(2\theta_i - 2\theta_k) P_k A + y_{bi} \quad (2.3)$$

where s stands for scale factor, k denotes the Miller indices, h, k, l, L_k includes the Lorentz, polarization, and multiplicity factors, Φ is the reflection profile function, P_k is the preferred orientation function, A is an absorption factor, F_k is the structure factor for the k^{th} Bragg reflection, and y_{bi} is the background intensity at the i^{th} step [61]. The Rietveld refinement technique is a structure refinement technique where prior knowledge of the basic structure is required in advance. However, efforts have been made to employ this technique to solve unknown structures [62]. In Rietveld method, different peak profile functions are available. Out of these, the pseudo-Voigt is the most commonly used. The pseudo-Voigt (pV) function is simply a linear combination of Lorentzian (L) and Gaussian (G) defined as [61]

$$pV = \eta L + (1-\eta)\, G \quad (2.4)$$

where, η is the pseudo-Voigt mixing parameter. The peak width is defined by full width at half maxima (FWHM) [63], [64]. The angular dependence of FWHM is expressed by the famous Coglioti function [65]:

$$(FWHM)^2 = U\tan^2\theta + V\tan\theta + W \quad (2.5)$$

where U, V and W are half-width parameters.

The Rietveld method involves refining a range of parameters, including parameters related to structure (position coordinates, unit cell parameters and thermal parameters), sample

parameters (strains, size of domain, preferred orientation), instrumental parameters (FWHM, origin shift, background etc.) and the scale factor. The refinable parameters are adjusted by successive iterative. The iteration is repeated until the best fit is obtained for calculated and observed pattern. There are various agreement factors used to define the quality of fit. They are referred to as various R-factors (or agreement factors), which are given as follows [66]–[69][61]:

(i) R- structure factor $:R_F=\frac{\sum|(I_K(`obs'))^{\frac{1}{2}}-I_K(cal)^{\frac{1}{2}})|}{\sum(I_k(`obs'))^{\frac{1}{2}}}$

(ii) R-profile factor $:R_p=\frac{\sum|y_{oi}-y_{ci}|}{\sum y_{oi}}$

(iii) R-Bragg factor $:R_B=\frac{\sum|I_K(`obs')-I_K(cal)|}{\sum(I_k(`obs'))}$

(iv) R-Weighted profile factor $:R_{wp}=\left\{\frac{\sum wi(y_i(obs)-y_i(cal))}{\sum w_i(y_i(obs))^2}\right\}^{1/2}$

(v) R-expected weighted profile factor $:R_{exp}=\left[\frac{(N-P)}{\sum w_i y2_{oi}}\right]^{1/2}$

Where I_K is the intensity of K_{th} Bragg's reflection after final iteration, N and P are the number of observations and variables.

The goodness-of-fit indicator 'S' can be given as

$$S=\frac{R_{WP}}{R_e}=\left[\frac{S_y}{(N-P)}\right]^{1/2} \quad (2.6)$$

The value of S depends on the quality of diffraction data. The goodness of fit of the system is also represented by an indicator called χ^2 and expressed as

$$\chi^2=S^2=\left[\frac{R_{wp}}{R_{exp}}\right]^2=\left[\frac{S_y}{(N-P)}\right] \quad (2.7)$$

2.4.3 Synchrotron x-ray diffraction

Synchrotron x-ray diffraction (SXRD) measurement has been performed for low-temperature structural analysis using Rietveld refinement of the obtained diffraction pattern. The data was collected at the P24 beamline at PETRA-III (DESY), Hamburg, Germany. The SXRD pattern was obtained using a 25 keV x-ray radiation source in a temperature range of 15K-140K.

2.4.4 Magnetic Measurements

SQUID Magnetometer

MPMS works on the principle of a Superconducting Quantum Interference Device (SQUID) sensor having two parallel Josephson Junctions, where two superconductors are separated by a thin insulating (weak link) layer that allows tunnelling of electrons. Since it uses a "SQUID": superconducting interferometer, this is why the MPMS family of instruments are called SQUID magnetometers. The magnetometer measures the extremely small change in magnetic flux associated with the movement of the sample through a superconducting detection coil, which is subsequently converted and measured in the form of current.

Magnetic measurements have been performed using the Magnetic Property Measurement System (MPMS), i.e. MPMS3 (Quantum Design, Inc U.S.A) at Centre Instrument Facility (CIF), IIT (BHU), India. MPMS3 magnetometer allows magnetization measurement in the temperature range of 1.8 K to 400 K using a cryostat based on ^{4}He. The device uses a superconducting magnet (a solenoid of superconducting wire) to subject samples to magnetic fields up to +/- 7 tesla (70 kOe). This magnetometer is highly sensitive (~10^{-8} emu). The

samples of the type film, bulk, crystals, and powder can be used for measurement. The AC susceptibility frequency ranges from 0.1 – 1000 Hz.

In our case, for the magnetic measurement, a powder sample was used. Temperature-dependent dc magnetization (M-T) of the samples was measured at an applied magnetic field of 100 and 1000 Oe in temperature ranging from 2-200 K with a sweep rate of 2 K/min. The experiments have been performed using standard protocols for zero field-cooled warming (ZFCW), field-cooled cooling (FCC) and field-cooled warming (FCW) measurements. The magnetization vs. field (M-H) measurements were performed. The ac susceptibility versus temperature measurement has been performed using ZFCW, FCC, and FCW protocol at different frequencies and applied magnetic fields at constant driving ac amplitude 3 Oe and temperature sweep rate 1 K/min.

2.4.5 x-ray photoelectron spectroscopy

The x-ray photoemission spectroscopy (XPS) (also known as electron spectroscopy for chemical analysis, ESCA) has been broadly used for the identification of elemental composition, the oxidation state of the constituent elements, valence band structure and ligand co-ordination by probing the surface of the specimen. It is a surface-sensitive technique so it essentially provides the relative composition of the constituent's elements present at/near (20 to 50 Å below the surface) in the surface regime. XPS technique works on the principle of Einstein's photoelectric effect. The process involves irradiating a monochromatic beam of photons (x-ray) on the surface of the compound, and a secondary beam of electrons is ejected by absorbing these photons from the materials. If an x-ray photon of energy, hν falls on the surface of the sample and, emission of an electron occurs when the core level electrons are

excited by this energetic x-ray photon. The kinetic energy (K.E.) of electrons emitted in such a situation is given by:

$$K.E. = h\nu - B.E. - \phi \quad (2.8)$$

Where B.E. is the binding energy of the ejected electron and ϕ is the work function. The kinetic energy of ejected core electrons is a function of binding energy and, thus, characteristic of the element present in the sample, and the XPS spectrum is designed as a variation of the number of ejected electrons with binding energy.

The XPS (x-ray photoemission spectroscopy) measurement was carried out using an Omicron multi-probe science system equipped with a hemispherical electron energy analyzer (EA 125) and a monochromatic x-ray source Al-K line with photon energy 1486.70 eV. The average base pressure was maintained at a value of 6.1×10^{10} torr with a power of 280 W.

2.4.6 Raman Spectroscopy

Raman spectroscopy is basically a structural characterization tool. The Raman spectrum is more sensitive to the lengths, strengths, and arrangement of bonds in a material than its chemical composition. It responds more to details of defects and disorders than to trace impurities and chemical imperfections.

An intense monochromatic light (electromagnetic radiation of single frequency) beam impinges on the sample. When electromagnetic radiation interacts with an atom/molecule, the electric field associated with incident radiation distorts the electron clouds that is forming chemical bonds in the sample, storing some energy. When this field is reversed as the wave passes, the distortion in the electron cloud is relaxed, and the stored energy is reradiated. Even

though the incident beam can be polarized, directing the electric field in a specific direction relative to sample, the scattered beam is reradiated in all directions, providing a variety of scattering geometries. Both elastic and inelastic types of scattering are possible. Most of the stored energy is reradiated at the same frequency as that of the incident exciting light (elastically scattered). This component is known as Rayleigh scattering and gives a strong central line in the scattering spectrum. However, a small portion of the stored energy is transferred to the sample itself, exciting the vibrational modes. The vibrational energies are deducted from the energy of the incident beam, and weak sidebands appear in the spectrum at frequencies less than that of the incident beam (inelastic scattering). These are the Raman lines. Their separation from the Rayleigh line is a direct measure of the vibrational frequencies of the sample. The reverse process also occurs. Existing vibrations that have been excited by thermal processes, can be annihilated by coupling with the incident beam and can add their energies to that of the source. These appear as sidebands at higher wavenumbers. The Raman process that excites molecular and crystal vibrations is called Stokes scattering; the process that annihilates existing vibrations is called anti-Stokes scattering. The two spectra are mirror images on opposite sides of the Rayleigh line [70].

Our study recorded room-temperature Raman spectra using a WITec alpha 300 Raman Spectrometer with an excitation wavelength of 532 nm.

2.4.7 UV-Visible absorption Spectroscopy

The ultraviolet-visible spectroscopy is an absorption/reflectance spectroscopy in the ultraviolet-visible region of the electromagnetic spectrum. It has been extensively used to study a material's light-absorbing capacity and to estimate its optical band gap. In a UV-visible

spectrophotometer, the integral component consists of a light source, a monochromator, a sample holder, and a photodetector to obtain the absorption spectrum followed by the sample illumination using light in the ultraviolet region. There are two possible optical arrangements, namely single beam and double beam. White light (polychromatic) from a light source is introduced into a monochromator and dispersed through a diffraction grating. It then emits light of a specific wavelength through the exit slit. For a single slit, I/I° is the transmittance where I° is the irradiated monochromatic light, and I is the intensity of the detected transmitted light. In the case of a double beam setup, I and I° can be simultaneously obtained by splitting the monochromatic light into two using a beam splitter and allowing these beams to pass through a reference and sample. The measured value is the ratio of intensities of the two beams.

Optical diffused reflectance spectra for $Dy_2Ti_{2-x}Mn_xO_7$ (x = 0.0, 0.05, 0.10, 0.15, 0.20) and $Er_2Ti_{2-x}Mn_xO_7$ (x = 0.0, 0.10, 0.20) polycrystalline samples in the range 220 - 1400 nm were collected at room temperature with a double beam UV-Visible spectrophotometer (SHIMADZU-2450). For reference purposes, a white standard of barium sulphate was used. The intensity of the beam that passes through the reference is considered 100% transmission or zero absorbance. Absorption spectra were derived from the reflectance data using the Kubelka – Munk function [71]. The energy band gap of the samples has been calculated using the value of the absorption coefficient in the Tauc equation.

2.4.8 Photoluminescence emission spectroscopy

Photoluminescence is emission after excitation by irradiation with electromagnetic radiation. Photoluminescence (PL) is an emission of a certain wavelength of light when the sample is

exposed to light through three main processes: excitation, relaxation, and emission. It is a non-destructive technique used to study the electronic states of various materials. In PL, when light of a certain wavelength is illuminated on a material, it gains energy by absorbing light and photoexcitation of the material takes place. This can be described as a transition from the ground state to an excited state of an atom or from the valence band to the conduction band of a semiconductor crystal (electron-hole pair creation). The electron loses its excess energy through non-radiative relaxation (does not produce light) while coming to the lowest energy state in the C.B. Subsequently, the electron falls back to the V.B. The energy lost is converted back into a luminescent photon emitted from the material. The intensity of this emitted photon is obtained as a function of wavelength. Hence, the direct measure of the band gap energy (E_g) is extracted from the energy of the emitted photon. This entire photon excitation followed by photon emission is termed photoluminescence.

Our study recorded Luminescence spectra using a Hitachi F-4600 Fluorescence spectrometer with a Xenon lamp as an excitation source.

2.4.9 Density Functional Theory

Density Functional Theory (DFT) is simply the "theory of the energy of electrons being functional of their density." It is a powerful technique to study the nanostructures, solids, surfaces and interfaces, and molecules by solving approximate versions of the Schrödinger equation. It is an alternative approach to the theory of electronic structure; electron density plays a central role in DFT. To understand material's properties at the atomic level, we can treat them as complicated collections of electrons and nuclei.

materials = electrons + nuclei

To understand the behaviour of quantum particles, we need to determine the corresponding wavefunction $\Psi(r)$ for every point $r = xu_x + yu_y + zu_z$ in the region of interest by solving a Schrödinger equation (Schrödinger, 1926). Here, u_x, u_y, and u_z denote the unit vectors along the Cartesian axes.

The time-independent Schrödinger equation takes the following symbolic form [72]:

$$(\text{Kinetic energy} + \text{potential energy})\ \Psi = E_{tot}\Psi \tag{2.9}$$

E_{tot} represents the system's total energy in the quantum state specified by the many-body wavefunction Ψ.

$$[p^2/2m_e + V(r)]\ \Psi(r) = E\ \Psi(r) \tag{2.10}$$

where m_e stands for electron mass, and the quantum-mechanical momentum operator is given by:

$$p = -i\ \hbar\ \nabla,\ \nabla = u_x\frac{\partial}{\partial x} + u_y\frac{\partial}{\partial y} + u_z\frac{\partial}{\partial z},$$

The kinetic energy to consider N electrons and M nuclei:

$$\text{Kinetic energy} = -\sum_{i=1}^{N}\frac{\hbar^2}{2m_e}\nabla_i^2 - \sum_{I=1}^{M}\frac{\hbar^2}{2M_I}\nabla_I^2. \tag{2.11}$$

In the case of derivatives in the Laplace operators, ∇^2 is taken with respect to the coordinates of each particle.

$$\nabla^2\Psi = \frac{\partial^2\Psi}{\partial x_1^2} + \frac{\partial^2\Psi}{\partial y_1^2} + \frac{\partial^2\Psi}{\partial z_1^2} \tag{2.12}$$

For the potential energy term, firstly, we have the Coulomb repulsion between electron pairs given as:

$$(\text{Potential energy})_{ec} = \tfrac{1}{2} \sum_{i \neq j} \frac{e^2}{4\pi\epsilon_\circ} \frac{1}{|r_i - r_j|} \tag{2.13}$$

Here, the indices *i* and *j* run from 1 to *N*. The term $i = j$ is excluded because an electron does not repel itself, and we divide by 2 to count only one contribution per pair.

Secondly, we have the Coulomb repulsion between pair of nuclei:

$$(\text{Potential energy})_{nn} = \tfrac{1}{2} \sum_{i \neq j} \frac{e^2}{4\pi\epsilon_\circ} \frac{Z_I Z_J}{|R_I - R_J|} \tag{2.14}$$

Here, the indices *I* and *J* run from 1 to *M,* and the Z_I represent the atomic numbers.

Third, we have the Coulomb attraction between electrons and nuclei:

$$(\text{Potential energy})_{nn} = - \sum_{i,I} \frac{e^2}{4\pi\epsilon_\circ} \frac{Z_I}{|r_i - R_I|} \tag{2.15}$$

with *i* from 1 to *N* and *I* from 1 to *M*. At this point, we can combine equations from 1 to 6 and write the many-body Schrödinger equation:

$$\left[- \sum_{i=1}^{N} \frac{\hbar^2}{2m_e} \nabla_i^2 - \sum_{I=1}^{M} \frac{\hbar^2}{2M_I} \nabla_I^2 + \tfrac{1}{2} \sum_{i \neq j} \frac{e^2}{4\pi\epsilon_\circ} \frac{1}{|r_i - r_j|} + \tfrac{1}{2} \sum_{i \neq j} \frac{e^2}{4\pi\epsilon_\circ} \frac{Z_I Z_J}{|R_I - R_J|} + - \sum_{i,I} \frac{e^2}{4\pi\epsilon_\circ} \frac{Z_I}{|r_i - R_I|}\right] \Psi = E_{tot} \Psi \tag{2.16}$$

From the US National Institute of Standards and Technology database, the values are as such:

$\hbar = 1.05457163 \times 10^{-34}$ Js

$m_e = 9.10938291 \times 10^{-31}$ kg,

$m_p = 1.67262164 \times 10^{-27}$ kg,

$e = 1.60217649 \times 10^{-19}$ C,

$\epsilon_0 = 8.85418782 \times 10^{-12}$ F/m

Now using,

1 Ha = 27.2114 eV = 4.3597×10^{-18} J,

1 bohr = 0.529177 Å = 0.529177×10^{-10} m,

1 a.u. of mass = $9.10938291 \times 10^{-31}$ kg,

where 'Ha' stands for Hartree and 'a.u.' for atomic unit. These units form the so-called Hartree atomic units. In Hartree atomic units, the many-body Schrödinger equation acquires the following elegant form:

$$[-\sum_i \frac{\nabla_i^2}{2} - \sum_I \frac{\nabla_I^2}{2M_I} + \tfrac{1}{2} \sum_{i \neq j} \frac{1}{|r_i - r_j|} + \tfrac{1}{2} \sum_{i \neq j} \frac{Z_I Z_J}{|R_I - R_J|} + -\sum_{i,I} \frac{Z_I}{|r_i - R_I|}] \Psi = E_{\text{tot}} \Psi \quad (2.17)$$

This is the most common form of the many-body Schrödinger equation in the first-principle study. In above equation, the only external parameters required are atomic numbers(Z_I), and the atomic masses (M_I).

Now, applying various approximations on this, namely clamped nucleus approximation, independent electron approximation, exclusion principle, mean-field approximation, and Hartree-Fock equations, we arrive at the Kohn-Sham equation:

$$[-\frac{\nabla^2}{2} + V_n(r) + V_H(r) + V_x(r) + V_c(r)] \varphi i(r) = \varepsilon_i \varphi_i(r) \quad (2.18)$$

Where V_n is the external nuclear potential, V_H is the Hartree potential and the kinetic energy term is given by $-1/2\nabla^2$,

$$V_n(\mathrm{r}) = -\sum_I \frac{Z_I}{|r - R_I|} \quad (2.19)$$

And Hartree potential is given as:

$$n(\mathrm{r}) = \sum_i |\Phi_i(r)|^2 \quad (2.20)$$

$$\nabla^2 V_H(r) = -4\pi n(r) \quad (2.21)$$

The above-described Kohn–Sham equations are central to the first principles of materials modelling. V_x and V_c are called the exchange and correlation potential given as:

$$V_{xc}(\boldsymbol{r}) = \delta E_{xc}[n]/\delta n \; |n(r)| \tag{2.22}$$

The external nuclear potential, kinetic energy and Hartree energy constitute the total energy in the independent electron approximation. The practical usefulness of ground-state DFT depends entirely on whether approximations for the functional $E_{xc}[n]$ could be found, which are at the same time sufficiently simple and accurate [73].

To incorporate such a functional, a convenient approach is studying the exchange and correlation energy of a simple system, the homogeneous electron gas. This system is closely related to the 'free electron gas' where electron gas is constrained within a box, and the nuclei potential is treated as constant. This approximation is known as local density approximation (LDA). The plane wave cut-off energy is given through LDA-1/2 approximation, where 1/2 of the electronic charge is subtracted from the ion's topmost orbitals [74]. The functional form of the exchange and correlation energy is further improved considering not only the density but also its gradients, and this approximation is called generalized gradient approximation (GGA).

In our study, the electronic structure calculation was carried out based on density functional theory (DFT) using a plane-wave basis set and pseudopotential as implemented in the Quantum-ESPRESSO package [75]. We used local density approximation (LDA) for exchange-correlation interactions. Rappe-Rabe-Kaxiras-Joannopoulos (RRKJ) flavor of ultra-soft pseudopotentials was used to represent the interaction between the ion cores and the valence electrons. The ground state electronic configurations used for the pseudopotential

generation of the constituent atoms were: Dy = [Xe] $4f^{9.0}5d^{1.0}6s^{1.5}$ $6p^{0.5}$, Ti = [Ar] $4s^2$ 4p0 $3d^2$, O = [He] $2s^2$, $2p^4$, Mn = [Ar] $^3d^{5.0}$ $4s^2$ $4p^0$, Er = [Xe] $4f^{11.0}$ $5d^{1.0}$ $6s^{1.5}$ $6p^{0.5}$. Scalar-relativistic pseudopotentials that account for most of the relativistic effects have been used, and spin-orbit coupling is excluded in the present calculation. Kinetic energy cut off of 70 Ry for wavefunction and 700 Ry for charge density, and a 6 × 6 × 6 k-point mesh for the Brillouin zone (BZ) integration was applied and was found to be sufficient for accurate calculation of electronic and structural properties. XCrySDen graphic software has been used for the structural visualization of this system.

In our modelling approach to the band structure, we went beyond standard DFT and used a method called LDA-1/2 technique which is based on Slater's transition state theory [76] since the standard DFT underestimates the band gap by as much as 50% or more. The LDA-1/2 technique is used to correct the self-energy contribution to the electronic excitation energy in the LDA-DFT. The self-interaction correction is carried out at the atomic pseudo potential level, thereby leading to solid-state calculations with a corrected band gap. This method, however, requires us to find the CUT radius (energy cut-off radius; energy that determines the size of the plane wave basis set) for each atomic pseudo potential for which the band gap of the system is optimal. The advantage of this method over the other known methods, such as the GW (which includes Green's Function G and screened Coulomb Interaction W) and the hybrid functional approaches, is that the calculation of the corrected band gap comes out with the computational cost of the standard LDA-DFT [77][74]. We used the LDA-1/2 pseudopotentials for Mn, Ti, and O atoms, whereas the Dy and Er pseudopotentials is of standard LDA functional.

So, this chapter summarizes the experimental tools' working principle and the measurement protocols followed to characterize the systems. The results of the structural and magnetic properties of Mn-doped $Dy_2Ti_2O_7$ are presented in the next chapter.